Tailoring Storage Capacity and Ion Kinetics in Ti_2CO_2/Graphene Heterostructures by Functionalization of Graphene

Cem Sevik[1] and Deniz Çakır[2,*]

[1] *Department of Mechanical Engineering, Faculty of Engineering, Anadolu University, Eskisehir, TR 26555, Turkey*

[2] *Department of Physics and Astrophysics, University of North Dakota, Grand Forks, North Dakota 58202, USA*

(Received 14 November 2018; revised manuscript received 25 April 2019; published 1 July 2019)

Using first-principles calculations, we evaluate the electrochemical performance of heterostructures made up of Ti_2CO_2 and chemically modified graphene for Li batteries. We find that heteroatom doping and molecule intercalation have a significant impact on the storage capacity and Li migration barrier energies. While N and S doping do not improve the storage capacity, B doping together with molecule interaction make it possible to intercalate two layers of Li, which stick separately to the surface of Ti_2CO_2 and B-doped graphene. The calculated diffusion-barrier energies (E_{diff}), which are between 0.3 and 0.4 eV depending on Li concentration, are quite promising for fast charge and discharge rates. Besides, the predicted E_{diff} as much as 2 eV for the diffusion of the Li atom from the Ti_2CO_2 surface to the B-doped graphene surface significantly suppresses the interlayer Li migration, which diminishes the charge and discharge rates. The calculated volume and lattice parameter changes indicate that Ti_2CO_2/graphene hybrid structures exhibit cyclic stability against Li loading and unloading. Consequently, first-principles calculations we perform evidently highlight the favorable effect of molecular intercalation on the capacity improvement of ion batteries.

DOI: 10.1103/PhysRevApplied.12.014001

I. INTRODUCTION

Developments in technological applications demand highly efficient and economic energy storage devices such as rechargeable Li-ion batteries (LIBs) [1,2]. The performance of Li-ion batteries is mainly determined by the electronic, structural, and mechanical properties of constituents including electrodes and electrolytes. In this respect, two-dimensional (2D) materials with unique chemical and electronic properties are emerging as effective electrode materials for the rechargeable lithium batteries with enhanced energy and power storage density to satisfy ever increasing demands of electronic devices and electrical vehicles including cars and drones [3]. Previous theoretical and experimental works suggest that loosely packed 2D sheets with a large interlayer spacing can provide enough volume between the layers to store metal ions and help to defy the structural instabilities confronted by bulk materials such as a large volume expansion during the charging and discharging cycle. Silicon anodes have been shown to undergo a volume change of 300% during lithiation and delithiation, resulting in capacity fading and limited cycle life due to severe particle pulverization, unstable solid-electrolyte interphase (SEI) formation and loss of electrical contact [4]. Therefore, 2D-based electrodes are free of such large volume expansions due to binding nature between the layers. In addition, 2D materials have a large surface area that can be utilized to enhance energy and power density of Li batteries [3,5,6]. Further enlargement of interlayer spacing obtained through intercalation of molecules between the 2D layers provides much higher accessibility to the active sites and lower diffusion barriers that are the most important for performing high-performance energy storage [7–9]. In a recent work, we found that a high lithium storage capacity and fast kinetics can be realized for $Ti_3C_2O_2$ multilayers by preintercalating organic molecules [10]. Therefore, intercalation appears as an effective structural and chemical engineering approach for improving electrochemical performance of batteries based on 2D materials.

Graphite and nongraphitic carbon are the dominant anode materials in Li-ion batteries. Graphite shows a reversible storage capacity of 372 mAh/g [2,11]. In spite of its excellent electrical conductivity, Li adsorption ability of graphene is poor. In a previous study, we showed that *MX*ene-graphene heterostructures exhibit a good compromise between storage capacity and kinetics for Li-battery applications [12]. In contrast to graphene, Li ions are strongly bind to oxygen-terminated *MX*ene. In addition, the presence of graphene in a heterostructure

*dcakir79@gmail.com

ensures a good electrical conductivity that is an essential requirement for battery applications. Similarly, diffusion-barrier calculations revealed the advantage of *MX*ene-graphene heterostructures over sole *MX*ene systems as the energy barriers are found to be significantly lower for alkaline and earth alkaline metals [12,13]. Previous studies have demonstrated that chemical modification is a promising way to enhance electrochemical performance of graphene sheet [14–20]. As an example, the charge and discharge capacity of N-doped graphene nanosheet increases with the charge and discharge cycles. It reaches 684 mAh/g in the 501st cycle, while it is only 452 mAh/g in the 100th cycle, showing higher cycling stability and larger specific capacity of N-doped graphene in comparison to a pristine graphene and a commercialized graphite anode. N-doped graphene layers prepared by using a chemical-vapor-deposition technique shows a Li storage capacity double that of pristine graphene due to the presence of a large number of surface defects [19]. Similarly, N- and B-doped graphene samples produced by using a mixed gas of NH_3BCl_3 and Ar can have a high reversible Li capacity of > 1040 mAh/g with a rate of 50 m/A, meaning a fast charging and discharging rate [20].

*MX*enes, new members of the 2D material family, have tunable electronic and thermal properties depending on their chemical composition and functionalization [21]. Their superior electrochemical and ion intercalation ability, very high electrical conductivity, and mechanical stability make them promising materials in technological applications including batteries [22–35], capacitors [36–38], hydrogen storage [39], electromagnetic interference shielding (EMI) [40], and electronic devices [41]. We prefer to combine graphene with *MX*ene due to the following reasons: (1) many of the *MX*ene crystals exhibit excellent metallic properties that are essential for battery applications [42,43]; (2) *MX*enes exhibits very good mechanical and dynamical stability [44]; (3) depending on the type of transition metal atom and surface termination, we can tune the chemical composition and structural varieties of *MX*enes.

In this work, we perform first-principles calculations based on density-functional theory (DFT) to evaluate the performance of heterostructure formed between chemically modified graphene and Ti_2CO_2 as an alternative electrode material for LIBs. By building heterostructures from stacking of dissimilar 2D sheets (such as *MX*ene and graphene in this work) and pillared structures through intercalation of molecules between 2D sheets, it is possible to combine the advantages and eliminate the disadvantages of the individual monolayers [5]. As a representative example, while Ti_2CO_2 contracts during ion intercalation, graphene expands. So, by combining graphene and *MX*ene, we can defy the significant expansion or contraction of the electrode, leading to an increased battery lifetime. Similarly, in graphite, the Li^+ intercalation follows a staging mechanism, where Li ions intercalate into specific interlayers at a time instead of random distribution into available empty interlayers. This process profoundly increases interlayer spacing and volume of the storage system [45]. In this respect, pillared structures can be used as an effective strategy to minimize the change in the interlayer distances in multilayers during ion loading and unloading. In this work, we aim to minimize interlayer expansion, and hence volume expansion, accompanying ion intercalation by introducing a benzene-based organic molecule within heterostructure. We consider the attachment of organic molecule to the graphene plane in order to fix it. This design principle helps to avoid diffusion of molecule together with Li ions, which may obstruct the Li migration. Moreover, we are able to realize a uniform interlayer separation between *MX*ene and B-doped graphene sheets. In addition to the molecule intercalation, heteroatoms are introduced into the graphene framework with the expectation that the surface adsorption energy of ions is changed, the ion diffusion barrier is reduced and thus the performance of the battery is enhanced. We explored the doping and intercalation effects on the adsorption, diffusion, and storage capability of Li within *MX*ene-graphene heterostructures.

II. COMPUTATIONAL METHOD

All calculations are performed within the framework DFT, as implemented in the Vienna *ab initio* simulation package (VASP) code [46,47]. The exchange-correlation interactions are treated using the generalized gradient approximation (GGA) within the Perdew-Burke-Ernzerhof (PBE) formulation [48]. The single electron-wave functions are expanded in plane waves with a kinetic energy cutoff of 400 eV. For the structure optimizations, the Brillouin-zone integrations are performed using a Γ-centered regular $5 \times 5 \times 1$ k-point mesh within the Monkhorst-Pack scheme [49]. The convergence criterion for electronic and ionic relaxations are set as 10^{-5} and 10^{-2} eV/Å, respectively. In order to minimize the periodic interaction along the z direction the vacuum space between the layers is taken at least 15 Å. We include van der Waals (vdW) interactions using the DFT-D3 method, including Becke-Jonson damping [50].

We calculate diffusion barriers for the Li atom using the climbing-image nudged-elastic band (CI NEB) method as implemented in the VASP transition-state tools [51,52]. CI NEB is an efficient method in determining the minimum energy-diffusion path between two given positions. We use a 3×3 and 5×5 supercell structures with nine images, including initial and final positions, for CI NEB calculations. The atomic positions and energy of the images are then relaxed. The amount of charge transfer between the Li atom and *MX*ene-graphene heterostructures is determined by using the Bader charge analysis [53–55].

III. RESULTS AND DISCUSSION

A. Energetic and structural properties of pristine and doped graphene

We first study the structural and electronic properties of pristine and doped graphene before investigating the considered graphene/Ti_2CO_2 heterostructures. In this work, we only consider graphitic B, N, and S. In other words, we replace a certain amount of C atoms with B or N or S without creating additional carbon vacancies near the substituent atoms. However, three different bonding configurations are possible for nitrogen in graphene, namely graphitic N, pyridiniclike N, and pyrrolic-type N. Some experiments showed that pyridinic N and graphitic N are dominant configurations [56]. In a recent work, it has been shown that a relatively low partial pressure of CH_4 (mixing with NH_3) can lead to the growth of dominant pyridinic N substitutions in graphene lattice. In contrast, the growth of dominant graphitic N substitutions can be realized under a higher partial pressure of CH_4 [57]. This and similar works undoubtedly point out that the doping type of N into the graphene lattice is able to be tuned by adjusting experimental growth conditions. Regarding the B doping of graphene, Kawai *et al.* showed that controllable doping of graphene is able to be achieved in atomic precision [58]. Similarly, in a recent work, it was shown that the reaction between benzene and boron tribromide in a closed reactor at elevated temperature (800 °C) leads to the synthesis of bulk boron-doped graphitic carbon [59].

In the 5×5 graphene supercell, as a representative example, only four carbon atoms are substituted, which corresponds to a chemical formula $C_{46}X_4$, and thus a 8% doping concentration (Fig. 1). Higher dopant concentrations increase the lattice mismatch between graphene and Ti_2CO_2. As an example, the lattice constant of pristine graphene increases from 2.46 to 2.59 Å when the B concentration becomes 33.3%, corresponding to a 5.2% lattice expansion. However, for a 8% doping concentration, such expansion is only 1.25%. We selected B, N, and S as substituents (or X), which have electronic configuration of [He]$2s^2 2p^1$, [He]$2s^2 2p^3$, and [Ne]$3s^2 3p^4$, respectively. The substituent atoms are well separated to minimize the strain effect due to size difference between C and substituent atoms. Akin to graphene, B- and N-doped graphene has almost planar structure. However, S-doped graphene exhibits a drastic deformation in the geometric structure such that each S atom forms a pyramidal-like bonding configuration with three carbon atoms. To minimize induced strain within the graphene lattice, half of the S atoms appear above the graphene plane, while the other half is connected from below. Figure 2 shows the density of states of pristine and doped graphene without Li. B- and N-doped systems exhibit metallic behavior, which is an essential requirement for battery applications. While B doping lowers the Fermi level (leading to p-type doping), N and S rise the Fermi level (giving rise to n-type doping). S doping significantly alters the electronic structure of graphene, opening a band gap with a value as much as 1 eV. A sharp peak mainly from the sulfur atoms emerges just below the Fermi level [Fig. 2(d)].

To understand the influence of substituent atom on Li adsorption, the binding energy of Li on pristine and doped

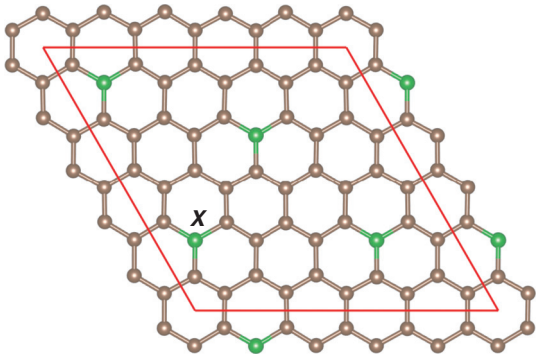

FIG. 1. Structure of a 5×5 graphene supercell that we use in our calculations. Green atoms (or X) are the substituent atoms.

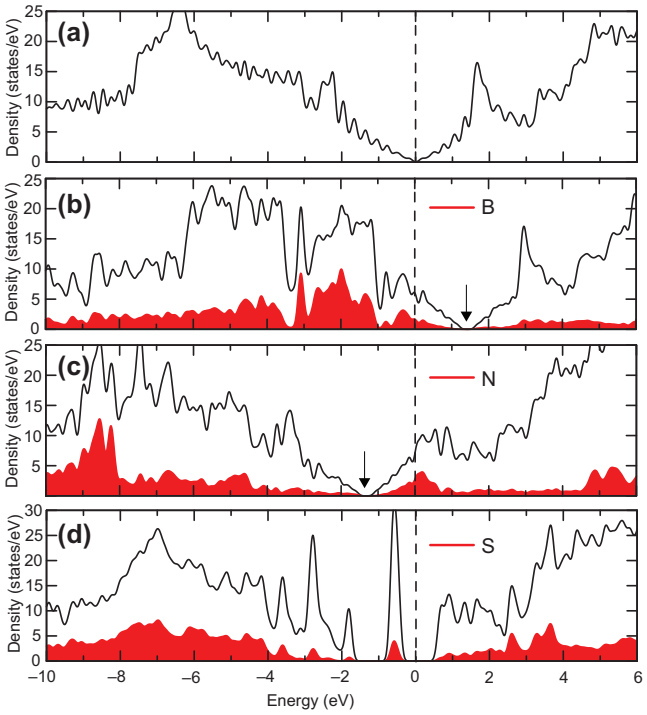

FIG. 2. Density of states (DOS) for (a) pristine, (b) B-doped, (c) N-doped, and (d) S-doped graphene. The DOS for the substituent atom is represented by red color and the vertical axis is multiplied by 4 to make the DOS visible. The arrow marks the Dirac point in doped systems. A small band gap emerges at the Dirac point of B- and N-doped graphene.

graphene is calculated using the following formula:

$$E_{\text{bind}} = E_{\text{tot}}[\text{C}_{46}X_4 + \text{Li}] - E_{\text{tot}}[\text{C}_{46}X_4] - \mu[\text{Li}], \quad (1)$$

where $E_{\text{tot}}[\text{C}_{46}X_4 + \text{Li}]$ and $E_{\text{tot}}[\text{C}_{46}X_4]$ are the total energies of either pristine or doped graphene before and after introducing Li atom, and $\mu[\text{Li}]$ is the chemical potential of Li bulk. As a benchmark, we first compute the binding energy of a single Li atom on pristine graphene (Table I). According to the above definition, E_{bind} is positive, meaning that adsorption of Li on pristine graphene is an endothermic reaction, in agreement with previous studies [60,61]. Positive E_{bind} renders graphene unsuitable for anode applications. Our findings indicate a strong effect of the type of substituent atom on Li adsorption. Introducing B into the graphene lattice leads to an electron-deficient system. The electrons in the boron—carbon bond are shifted towards the more electronegative carbon atom. There are empty states above the valence band (Fig. 2). As Li is placed close to B-doped graphene, it tends to donate its $2s^1$ electron to this electron-deficient system. Here, B-doped graphene acquires charge from Li atom, and subsequently strongly attracts positively charged Li ion, enhancing adsorption ability of graphene. The absorbed Li atom stays close to hexagon with the B atom. The calculated binding energy for this adsorption structure is −1.12 eV. B doping also affects the Li binding on C hexagons, which are well separated from B atoms, with an average binding energy of −0.90 eV. N doping results in electron-rich systems, which do not tend to accept electron from Li atoms. Li binding on N-doped (S-doped) graphene is energetically less (slightly more) favorable as compared to pristine graphene. Bader charge analysis showed that the amount of charge transfer from Li to the host layer is $0.99e$ in B-doped graphene.

Experiments have shown an enhanced electrochemical storage performance of N-doped graphene with respect to undoped (or bare) one [18]. However, in this work, we find that graphitic N does not promise an enhanced storage performance for graphene due to unfavorable binding of Li on N-doped graphene. Our calculations reveal that p-type doping of graphene improves the adsorption of Li ion on graphene. A possible reason for the experimentally observed enhanced performance in N-doped graphene can be due to the presence of C vacancies and pyridinic N in the graphene network [62,63]. Introducing pyridinic N atoms into graphene lattice gives rise to p-type doping, which is a suitable method to enhance the electrochemical performance of graphene. Similarly, the carbon vacancy site on graphene plane is shown to serve as an attractive center for the ion, such as Li, adsorption on graphene. Computational calculations also suggest that nitrogen-decorated single- and double-vacancy defects in graphene appear as a promising candidate system for Li-ion batteries [64]. However, simulations for C vacancies together with pyridinic N require much larger simulation cells to minimize the lattice mismatch with the Ti_2CO_2 sheet and to ascertain the impact of the isolated vacancy+pyridinic N complex on the electrochemical properties of chemically modified graphene. Therefore, in the present study, we only consider graphitic B and N.

TABLE I. Binding energy of a Li ion on pristine and doped graphene in eV. @Dopant (@Carbon) means that Li is close to (away from) the substituent atom. The average C–C and C-substituent bond lengths are given in Å.

System	@Dopant	@Carbon	C–C	C-substituent
Pristine		+0.50	1.42	
B-doped	−1.12	−0.90	1.41–1.45	∼ 1.50
N-doped	+1.05	+0.88	1.41–1.43	∼ 1.41
S-doped	+0.44	+0.76	1.41–1.45	∼ 1.75

B. Energetic and structural properties of *MX*ene-functionalized graphene heterostructures

We construct a *MX*ene-graphene heterostructure from a 4×4 supercell of Ti_2CO_2 and a 5×5 supercell of graphene to minimize lattice mismatch between the layers. To find out the lowest energy stacking structure, we displace the Ti_2CO_2 layer over graphene and calculate the total energy of the whole system. The interlayer separation for the ground-state stacking structure is found to be around 3 Å measured between graphene and O layer of Ti_2CO_2. Then, the interface model of several structures shown in Fig. 3 are constructed to show the effect of functionalization of graphene on the Li storage capacity and kinetics. For the sake of brevity, we only scrutinize B-doped systems.

Because of the electron-rich character of N- and S-contained hexatomic rings, N and S doping are not beneficial to enhance electrochemical performances of *MX*ene-functionalized graphene heterostructures. In a previous work, we showed that only one monolayer of Li is able

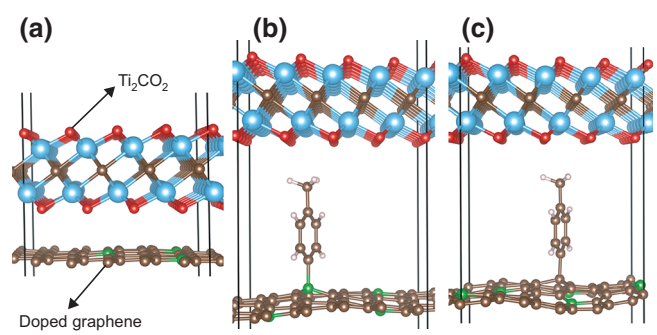

FIG. 3. Schematic representation of a *MX*ene and B-doped graphene heterostructure (a) without and (b),(c) with an intercalated molecule.

to be intercalated within a Ti_2CO_2/graphene heterostructure. In order to facilitate a much better performance, we chemically dope graphene to enhance storage capacity and easy Li diffusion. In the Ti_2CO_2/graphene heterostructure, we first substitute 8% of C atoms with B. The resulting structure has an interlayer separation of 2.83 Å [Fig. 3(a)]. In addition to this structure, B-doped graphene is also functionalized with molecules to enlarge interlayer spacing within the *MX*ene-graphene heterostructure as shown in Fig. 3(b). Here, the molecule prefers to stick to the graphene sheet through a C—B bond (with a bond length of, d_{C-B}, 1.68 Å) instead of a C—C bond (d_{C-C} = 1.58 Å). The former is found to be 0.70 eV energetically favorable. However, the latter structure is able to be obtained through attaching the molecule to the graphene sheet prior to B doping. We also compare the stability of the *MX*ene and B-doped graphene bilayer with and without molecules by calculating the formation energies, which are obtained using the computed total energy values of the *MX*ene and B-doped graphene bilayer with and without molecules, *MX*ene sheet, and B-doped graphene sheet with and without molecules. The formation energy is found to be 0.33 eV/cell or (2.3 meV/atom) for the *MX*ene and B-doped graphene bilayer with molecules, implying that the interaction between *MX*ene and chemically modified graphene is a weak van der Waals interaction. Due to the extended interlayer separation shown in Figs. 3(b) and 3(c), the binding energy between two monolayers is significantly small relative to the *MX*ene/B-doped graphene heterostructure without molecules denoted in Fig. 3(a) (23 meV/atom).

To assess the stability of Li adsorption within the Ti_2CO_2/graphene hybrid structure, the binding energies are calculated via the following expression:

$$E_{\text{bind}} = (E_{\text{tot}}[MX - C_{46}X_4 + n_{\text{Li}}\text{Li}] - E_{\text{tot}}[MX - C_{46}X_4] - \mu[\text{Li}])/n_{\text{Li}}, \quad (2)$$

where $E_{\text{tot}}[MX - C_{46}X_4 + \text{Li}]$ and $E_{\text{tot}}[MX - C_{46}X_4]$ are the total energies of *MX*ene-graphene heterostructures before and after introducing the Li atom. n_{Li} is the number of Li atoms. Several possible Li adsorption sites are considered to find out the lowest energy adsorption structure of a single Li atom. It is expected that heteroatom doping can significantly change the electrochemical storage properties of graphene due to varying electronegativity difference of atoms. Regardless of structural model of heterostructure, the Li atom strongly binds to the Ti_2CO_2 monolayer with an average binding energy of −1.80 eV. Expect B-doped graphene, the Li atom does not stick to the graphene sheet when using Li bulk chemical potential (Table II).

Figure 4 shows the variation of binding energy as a function of the number of intercalated Li atoms. At first glance, the Li binding energy decreases with increasing Li concentration for the reason that repulsive interaction between Li ions makes adsorption less energetic. The rate of change of the binding energy is slower for a hybrid structure without molecules. In addition, B-doped graphene strengthens the interfacial Li binding by 0.3–0.5 eV in this structure (red curve in Fig. 4)

TABLE II. Binding energy of a single Li ion on *MX*ene (@*MX*ene) and doped graphene with molecule in eV. There are two distinct adsorption sites on doped graphene, namely @Gr-substituent and @Gr-carbon. The former (latter) means that Li is close to hexatomic ring with (without) substituent.

System	@*MX*ene	@Gr-substituent	@Gr-carbon
B-doped *MX*-GR	−1.80	−1.23	−0.95
N-doped *MX*-GR	−1.78	+0.84	+0.60
S-doped *MX*-GR	−1.70	+0.52	+0.57

Figure 5 shows the DOS for the pristine and Li intercalated Ti_2CO_2/graphene heterostructure with molecules. In the pristine system, the Fermi level appears at the bottom of the conduction band of the *MX*ene layer. Occupying all available sites with Li on the *MX*ene surface, the Fermi level moves into the conduction band of *MX*ene [Fig. 5(b)]. The DOS of graphene is almost intact, meaning that there is only charge transfer between Li atoms and *MX*ene. The calculated average Bader charge is almost +1 on Li ions, implying a complete charge transfer. Once all the active sites on *MX*ene are occupied, the forthcoming Li ions prefer to bind to the graphene sheet and concomitant charge transfer only occurs between Li and graphene [Fig. 5(c)]. The calculated Bader charge is still very close to +1 for Li ions. The DOS of graphene shows about 1 eV rising of the Fermi level as a result of charge transfer.

Figure 6 shows the DOS for the pristine and fully lithianated Ti_2CO_2/graphene heterostructure without

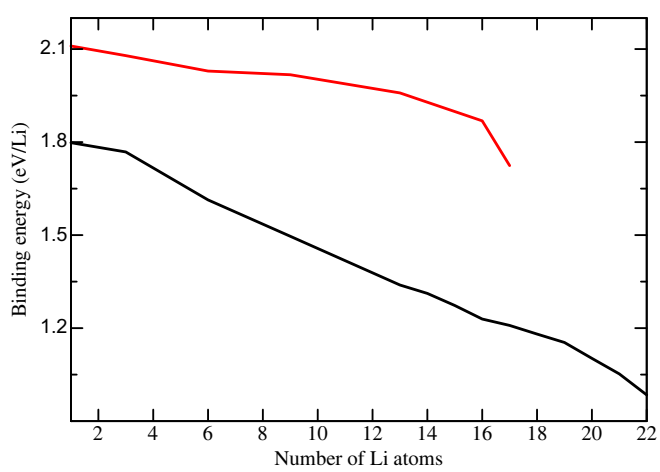

FIG. 4. Binding-energy variation as a function of Li concentration. Red (black) curve denotes binding-energy variation for the *MX*ene-functionalized graphene heterostructure without (with) molecules.

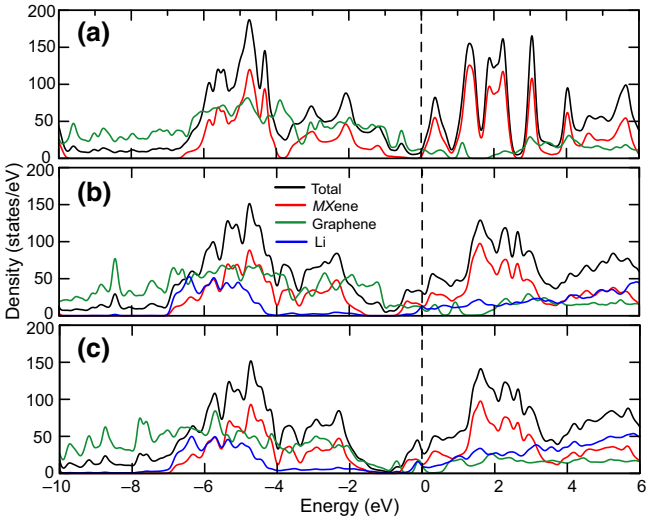

FIG. 5. Partial DOS (PDOS) of a (a) pristine, (b) partially, and (c) fully lithiated *MX*ene-functionalized graphene heterostructure with molecules. The vertical axis for graphene and Li is multiplied by 4 and 20, respectively, to make the DOS curves visible. The Fermi level shown by a black dashed line is at zero energy.

molecules. As is evident from Fig. 6(b), both *MX*ene and graphene sheets accept charges from intercalated Li ions. The Fermi level moves into the conduction band of *MX*ene and graphene. The average charge on Li ions is almost +1.

C. Li intercalation and average intercalation voltage

Next, the intercalation of Li atoms into *MX*ene-functionalized graphene is investigated. Only one face of graphene and *MX*ene are exposed to lithium adsorption to show the role of substituent atoms and molecule on the Li intercalation ability between *MX*ene and functionalized graphene. The lithiation reaction can be written as

$$MX/f\mathrm{GR}/\mathrm{Li}_x + n\mathrm{Li} \rightarrow MX/f\mathrm{GR}/\mathrm{Li}_{x+n}, \qquad (3)$$

where $MX/f\mathrm{GR}/\mathrm{Li}_x$ denotes the *MX*ene-functionalized graphene heterostructure with x Li atoms adsorbed. Using this reaction, in order to determine the maximum storage capacity of each system, the average intercalation voltage is calculated according to the following expression [32]:

$$V = -(E_{\mathrm{tot}}[MX/f\mathrm{GR}/\mathrm{Li}_{x+n}] - E_{\mathrm{tot}}[MX/f\mathrm{GR}/\mathrm{Li}_x] - nE_{\mathrm{tot}}[\mathrm{Li}])/en, \qquad (4)$$

where $E_{\mathrm{tot}}[MX/f\mathrm{GR}/\mathrm{Li}_{x+n}]$ and $E_{\mathrm{Tot}}[MX/f\mathrm{GR}/\mathrm{Li}_x]$ are the total energy of heterostructures with $x+n$ and n Li atoms, respectively. e is the absolute value of electron charge. The open-circuit voltage is one of the key factors, which is widely calculated to characterize the performance of a battery. Before calculating V, we first search the most stable Li adsorption configuration for each Li concentration. Figure 4 is plotted using the lowest energy adsorption configuration at each Li concentration. Owing to strong interaction of Li^+ ions with the Ti_2CO_2 surface, Li atoms first prefer to occupy all 16 active sites on the *MX*ene sheet. Then, doped graphene starts to accept Li ions until V becomes negative at which Li clustering is energetically favorable. For the *MX*ene-functionalized graphene heterostructure with molecules (Fig. 7), the lithiation starts at a voltage of around 1.79 V. This value is very close to the intercalation voltage of the Ti_2CO_2/pristine graphene heterostructure (approximately 1.7 V), meaning that Li intercalation voltage is mainly determined by Ti_2CO_2 [12]. As the 17th atom is intercalated very close to the Li layer (which is absorbed on the surface of Ti_2CO_2), the repulsive interaction due to preadsorbed Li^+ ions repels this

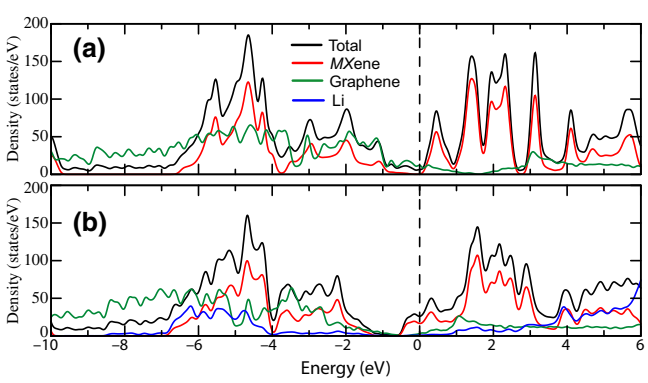

FIG. 6. PDOS of (a) pristine and (b) fully lithiated *MX*ene-functionalized graphene heterostructure without molecules. The vertical axis for graphene and Li is multiplied by 4 and 20, respectively, to make the DOS curves visible. The Fermi level shown by a black dashed line is at zero energy.

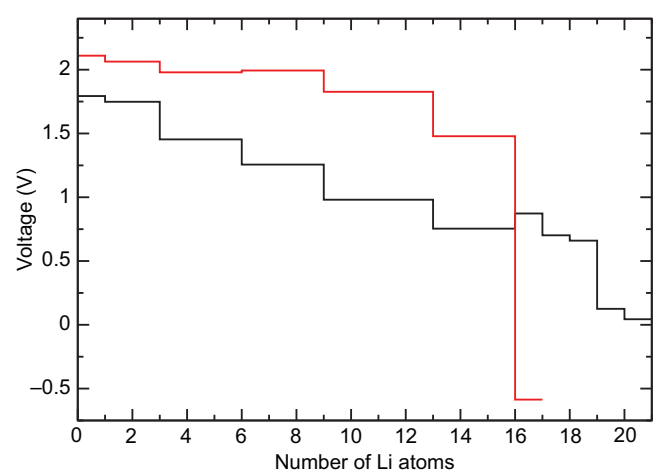

FIG. 7. Variation of average intercalation voltage as a function of Li concentration. Black (red) denotes voltage for the *MX*ene-functionalized graphene heterostructure with (without) molecules.

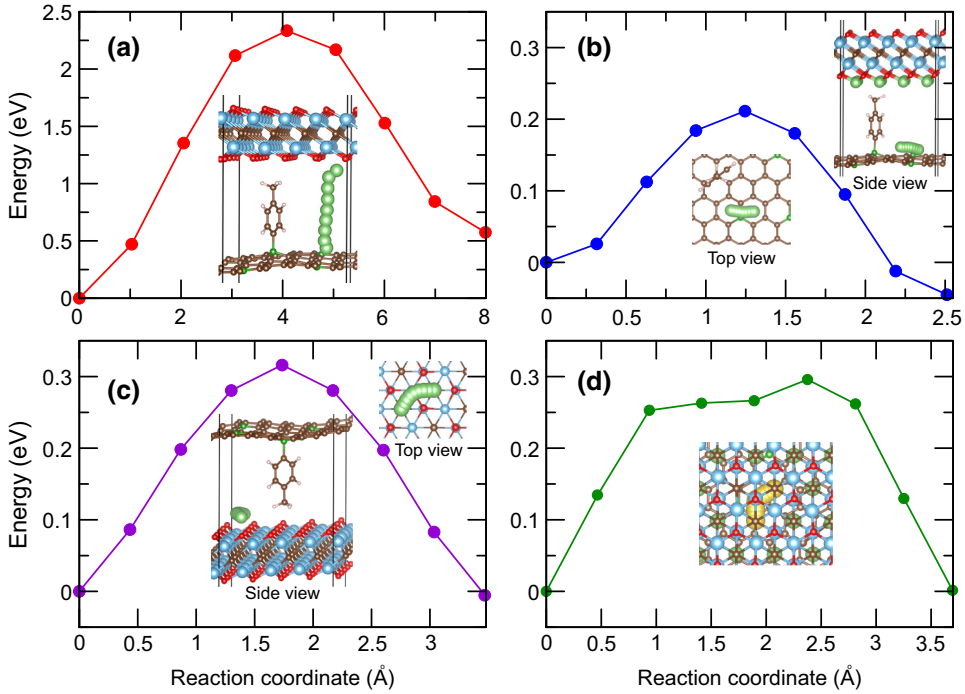

FIG. 8. Diffusion energy profiles and corresponding migration paths for the selected systems. In (d), the migrating Li atom is denoted by yellow color.

additional Li from the Ti_2CO_2 surface. However, depending on the type of substituent atom, the intercalation of the second layer is also possible. We demonstrate that the absorption of the second layer is an exothermic reaction for only B-doped graphene with molecules, whereas it is endothermic for other systems. In other words, clustering of Li atoms is energetically favorable for the latter systems. In this respect, introducing B atoms and molecules into the graphene lattice significantly enhances the storage capacity. Positively charged Li ions in the second layer tend to aggregate around B atoms. Each B atom can attract only one Li atom. Interestingly, interlayer expansion without B doping is not sufficient to realize Li adsorption on graphene. Here, the role of B doping is to create active sites on graphene framework, which are the most important for Li storage. In our *MX* ene-functionalized graphene heterostructure, we have a chemical formula of $C_{46}B_4Li_4$ (or $C_{11.5}BLi$). B-doped graphene (with molecule) starts to determine the intercalation potential as the number of Li atoms exceeds 16. Here, we only consider one side adsorption to explore the impact of the interface formation between dissimilar materials, doping of graphene and molecule intercalation on Li-storage performance and kinetics. For multilayer graphene, the maximum storage capacity is C_6Li [65]. To further increase the storage capacity, the B-atom concentration should be increased. Adsorption of the 17th Li increases the lithiation voltage from 0.57 to 0.87 V. Such an increase in voltage is attributed to an energy gain due to the adsorption of the 17th Li on B-doped graphene. Then, subsequent addition starts to lower the voltage. It drops to 0.70 V for the 18th Li, 0.66 V for the 19th Li, 0.12 V for the 20th, and 0.04 V for the 21th Li atoms. When the number of Li ions exceeds 21, the lithiation voltage becomes negative, meaning that Li atoms tend to form clusters rather than staying isolated. The calculated cell voltage averaged for compositions between fully lithiated and unlithiated states is 1.05 V, which falls into electrochemical windows of different pertinent electrolytes [1].

Another important benefit of doping and intercalation is that the average intercalation voltage is able to be tuned by modifying heterostructure design. Enlargement of the interlayer spacing through intercalation of molecules tends to reduce intercalation potential. The calculated average voltage for the *MX* ene-functionalized graphene heterostructure without molecules is shifted upward by around 0.3–0.5 V as compared to that for the *MX* ene-functionalized graphene heterostructure with molecules. The *MX* ene-functionalized graphene heterostructure without molecules has a slower decrease rate of the intercalation potential in accordance with the variation of binding energy shown in Fig. 4.

Theoretical gravimetric capacity, C (mAh/g), at maximum Li concentration ($x_{\max}$) is computed using

$$C = \frac{x_{\max} \times z \times F \times 10^3}{M_{\text{pillar}}}, \tag{5}$$

TABLE III. Calculated diffusion barriers for several migration paths in eV. Barrier 1 is the diffusion barrier of a single Li ion on *MX*ene sheet, corresponding to $x = 0.05$ [Fig. 8(c)]. Barrier 2 (barrier 3) denotes the diffusion barrier of a single Li ion for the concentration of $x = 0.88$ (0.94) on the *MX*ene sheet. Figure 8(d) shows the migration path for barrier 2. Barrier 4 [Fig. 8(b)] is the diffusion barrier of a single Li ion on B-doped graphene for $x = 0.05$. Finally, barrier 5 [Fig. 8(a)] represents the diffusion of a single Li ion from the *MX*ene sheet to B-doped graphene sheet.

Barrier 1 @*MX*ene ($x = 0.05$)	Barrier 2 @*MX*ene ($x = 0.90$)	Barrier 3 @*MX*ene ($x = 0.95$)	Barrier 4 @Gr ($x = 0.05$)	Barrier 5 *MX*ene → Gr
0.32	0.30	0.72	0.21	2.33

where z is the valence number of Li, F is the Faraday constant (26.81 Ah/mol) and M_{pillar} is the atomic mass of pillared structure including Li atoms as well. Here, we assume a bulk structure such that both surfaces of graphene and Ti_2CO_2 sheets accept Li ions. The calculated C is 350.3 mAh/g, which is much larger than C of pristine Ti_2CO_2 (182.8 mAh/g) and the Ti_2CO_2/pristine graphene heterostructure (280.5 mAh/g) [12].

D. Diffusion barriers

In addition to stability and high storage capacity, a good rate performance is required for an excellent battery application. The rate performance is controlled by electronic and ionic transport. Even though we do not calculate the electron transport properties of heterostructures, the calculated DOS plots confirm that our structures display metallic properties before and after Li adsorption. In addition, the presence of lightly doped graphene ensures a good electrical conductivity in our heterostructures. We calculate the migration energy barriers (E_{diff}) along several pathways using the CI NEB method. Figure 8 shows the barrier energies and corresponding pathways for the selected concentrations. At first glance, it can be seen that the calculated barrier energies are lower for the *MX*ene-functionalized graphene heterostructure as compared to commercial electrodes. At a dilute Li concentration, E_{diff} is around 0.25–0.32 eV for the on-plane Li diffusion. In contrast, we find a very large diffusion-barrier energy for the out-of-plane diffusion. This means that once a Li atom is adsorbed on either *MX*ene or graphene, it most likely stays there. We also compute E_{diff} for two different high Li concentrations. While we only have one Li vacancy in the first configuration, two nearby Li vacancies are created in the second case on the surface of Ti_2CO_2. These two configurations give rise to totally different barrier energies. Figure 8(d) displays the barrier energy profile and path for the two-vacancy structure ($x = 0.90$). Here, E_{diff} is around 0.3 eV and not much different than that of structures with a single Li atom absorbed [Fig. 8(c)]. However, the single-vacancy structure results in an E_{diff} of 0.72 eV ($x = 0.95$). Our calculations imply two main regimes for ion transport. Up to Li content of $x = 0.90$, E_{diff} is low. When x exceeds 0.90, E_{diff} increases substantially. This is due to a steric effect that obstructs the diffusion of Li^+ in the single-vacancy case (i.e., $x > 0.90$). In the two-vacancy case ($x < 0.90$), there is enough space for migrating Li ion to avoid nearby Li^+ ions. Interestingly, the diffusion barrier of a single Li atom between Ti_2CO_2 and B-doped graphene without molecules is around 0.30 eV, which is comparable with the heterostructure with molecules. This is due to the fact that we can weaken the strong effect of geometric constraint that is present in pristine multilayers by constructing heterostructures. Table III summarizes the barrier energies for several paths with different Li concentrations.

E. Cycling stability

We determine interlayer separation, lattice parameter and volume changes during the Li intercalation and deintercalation to test cyclic stability of *MX*ene-functionalized graphene heterostructures. First of all, we find no bond breaking. The C—B bond connecting molecules to graphene becomes 1.67 Å for a fully lithiated state with a change of −1.1% as compared to unlithiated state. The in-plane lattice parameters shrink only 0.5%. Due to the enlarged lattice spacing, all active sites are easily reachable by Li ions without any need for a large interlayer expansion. The total expansion along the vertical direction is around 6.5% (measured from unexposed O layer of Ti_2CO_2 to graphene layer), which is smaller than that of graphite (10%).

IV. CONCLUSION

In this work, we demonstrate that heterostructures made up of *MX*ene and functionalized graphene are promising candidate structures to control and manipulate the generation and diffusion of Li ions within interface of dissimilar materials. We chemically modify the graphene sheet with B and molecules. While the role of molecules is to enlarge interlayer distance, B doping is utilized to introduce active sites on the graphene sheet to enhance storage capacity. B doping significantly enhances Li binding on graphene. Molecule intercalation (i.e., interlayer expansion) is mandatory to make use of B doping for gravimetric capacity improvement. It turns out that the *MX*ene-functionalized graphene heterostructures provide a good electrical conductivity and low diffusion barriers as evidenced from band structure and migration energy calculations. We can realize diffusion barriers as low as

0.3 eV even for high Li concentrations. The out-of-plane diffusion barriers are at least six times larger than in-plane diffusion barriers, thus implying that Li ions move laterally on either the *MX*ene or graphene plane. As compared to pristine *MX*ene multilayers and *MX*ene-functionalized graphene without molecules, an enhanced storage capacity is able to be achieved with a value of 350.3 mAh/g for *MX*ene-functionalized graphene with molecules. Combining graphene with *MX*ene markedly limits the volume change that is critical to eliminate restacking and maintain a cyclic stability.

ACKNOWLEDGMENTS

Computer resources used in this work are provided by Computational Research Center (HPC-Linux cluster) at University of North Dakota, the High Performance and Grid Computing Center (TRGrid e-Infrastructure) of TUBITAK ULAKBIM, and the National Center for High Performance Computing (UHeM) of Istanbul Technical University. A part of this work is supported by University of North Dakota Early Career Award (Grant No. 20622-4000-02624). We also acknowledge financial support from ND EPSCoR through NSF Grant OIA-1355466. C. S. acknowledges the support from the TUBITAK (116F080) and the BAGEP Award of the Science Academy. This work is performed, in part, at the Center for Nanoscale Materials, a U.S. Department of Energy Office of Science User Facility, and supported by the U.S. Department of Energy, Office of Science, under Contract No. DE-AC02-06CH11357. C. S. acknowledges the support from the WOS (192070) program to attend program review meetings providing valuable discussion opportunities regarding this study.

[1] J. B. Goodenough and Y. Kim, Challenges for rechargeable Li batteries, Chem. Mater. **22**, 587 (2010).

[2] J.-M. Tarascon and M. Armand, Issues and challenges facing rechargeable lithium batteries, Nature **414**, 359 (2001).

[3] B. Anasori, M. R. Lukatskaya, and Y. Gogotsi, 2D metal carbides and nitrides (MXenes) for energy storage, Nat. Rev. Mater. **2**, 16098 EP (2017).

[4] Y. Jin, B. Zhu, Z. Lu, N. Liu, and J. Zhu, Challenges and recent progress in the development of Si anodes for lithium-ion battery, Adv. Energy. Mater. **7**, 1700715 (2017).

[5] E. Pomerantseva and Y. Gogotsi, Two-dimensional heterostructures for energy storage, Nat. Energy **2**, 17089 EP (2017).

[6] T. Kocabas, A. Ozden, I. Demircioglu, D. Cakir, and C. Sevik, Determination of dynamically stable electrenes toward ultrafast charging battery applications, J. Phys. Chem. Lett. **9**, 4267 (2018).

[7] J. Mei, Y. Zhang, T. Liao, Z. Sun, and S. X. Dou, Strategies for improving the lithium-storage performance of 2D nanomaterials, Natl. Sci. Rev. **5**, 389 (2018).

[8] P. Simon, Two-dimensional MXene with controlled interlayer spacing for electrochemical energy storage, ACS Nano **11**, 2393 (2017).

[9] J. Luo, W. Zhang, H. Yuan, C. Jin, L. Zhang, H. Huang, C. Liang, Y. Xia, J. Zhang, Y. Gan, and X. Tao, Pillared structure design of MXene with ultralarge interlayer spacing for high-performance lithium-ion capacitors, ACS Nano **11**, 2459 (2017).

[10] E. M. D. Siriwardane, I. Demiroglu, C. Sevik, and D. Cakir, Achieving fast kinetics and enhanced Li storage capacity for $Ti_3C_2O_2$ by intercalation of quinone molecules, ACS Appl. Energy Mater. **2**, 1251 (2019).

[11] J. R. Dahn, T. Zheng, Y. Liu, and J. S. Xue, Mechanisms for lithium insertion in carbonaceous materials, Science **270**, 590 (1995). http://science.sciencemag.org/content/270/5236/590.full.pdf.

[12] Y. Aierken, C. Sevik, O. Gulseren, F. M. Peeters, and D. Cakir, Mxenes/graphene heterostructures for Li battery applications: A first principles study, J. Mater. Chem. A **6**, 2337 (2018).

[13] I. Demiroglu, F. M. Peeters, O. Gulseren, D. Cakir, and C. Sevik, Alkali metal intercalation in MXene/graphene heterostructures: A new platform for ion battery applications, J. Phys. Chem. Lett. **10**, 727 (2019).

[14] X. Wang, Q. Weng, X. Liu, X. Wang, D.-M. Tang, W. Tian, C. Zhang, W. Yi, D. Liu, Y. Bando, and D. Golberg, Atomistic origins of high rate capability and capacity of N-doped graphene for lithium storage, Nano Lett. **14**, 1164 (2014).

[15] Y. Yang, D.-M. Tang, C. Zhang, Y. Zhang, Q. Liang, S. Chen, Q. Weng, M. Zhou, Y. Xue, J. Liu, J. Wu, Q. H. Cui, C. Lian, G. Hou, F. Yuan, Y. Bando, D. Golberg, and X. Wang, Protrusions or holes in graphene: Which is the better choice for sodium ion storage? Energy Environ. Sci. **10**, 979 (2017).

[16] L. Zhou, Z. F. Hou, B. Gao, and T. Frauenheim, Doped graphenes as anodes with large capacity for lithium-ion batteries, J. Mater. Chem. A **4**, 13407 (2016).

[17] Y. Liu, V. I. Artyukhov, M. Liu, A. R. Harutyunyan, and B. I. Yakobson, Feasibility of lithium storage on graphene and its derivatives, J. Phys. Chem. Lett. **4**, 1737 (2013).

[18] X. Li, D. Geng, Y. Zhang, X. Meng, R. Li, and X. Sun, Superior cycle stability of nitrogen-doped graphene nanosheets as anodes for lithium ion batteries, Electrochem. Commun. **13**, 822 (2011).

[19] A. L. M. Reddy, A. Srivastava, S. R. Gowda, H. Gullapalli, M. Dubey, and P. M. Ajayan, Synthesis of nitrogen-doped graphene films for lithium battery application, ACS Nano **4**, 6337 (2010).

[20] Z.-S. Wu, W. Ren, L. Xu, F. Li, and H.-M. Cheng, Doped graphene sheets as anode materials with superhigh rate and large capacity for lithium ion batteries, ACS Nano **5**, 5463 (2011).

[21] M. Naguib, V. N. Mochalin, M. W. Barsoum, and Y. Gogotsi, 25th anniversary article: MXenes: A new family of two-dimensional materials, Adv. Mater. **26**, 992 (2014).

[22] M. Naguib, O. Mashtalir, J. Carle, V. Presser, J. Lu, L. Hultman, Y. Gogotsi, and M. W. Barsoum, Two-dimensional transition metal carbides, ACS Nano **6**, 1322 (2012).

[23] Y. Sun, D. Chen, and Z. Liang, Two-dimensional MXenes for energy storage and conversion applications, Mater. Today Energy **5**, 22 (2017).

[24] B. Anasori, M. R. Lukatskaya, and Y. Gogotsi, 2D metal carbides and nitrides (MXenes) for energy storage, Nat. Rev. Mater. **2**, 16098 (2017).

[25] C. Eames and M. S. Islam, Ion intercalation into two-dimensional transition-metal carbides: Global screening for new high-capacity battery materials, J. Am. Chem. Soc. **136**, 16270 (2014).

[26] Y. Xie, M. Naguib, V. N. Mochalin, M. W. Barsoum, Y. Gogotsi, X. Yu, K.-W. Nam, X.-Q. Yang, A. I. Kolesnikov, and P. R. C. Kent, Role of surface structure on Li-ion energy storage capacity of two-dimensional transition-metal carbides, J. Am. Chem. Soc. **136**, 6385 (2014).

[27] M. Naguib, J. Come, B. Dyatkin, V. Presser, P.-L. Taberna, P. Simon, M. W. Barsoum, and Y. Gogotsi, MXene: A promising transition metal carbide anode for lithium-ion batteries, Electrochem. Commun. **16**, 61 (2012).

[28] Z. Lin, D. Sun, Q. Huang, J. Yang, M. W. Barsoum, and X. Yan, Carbon nanofiber bridged two-dimensional titanium carbide as a superior anode for lithium-ion batteries, J. Mater. Chem. A **3**, 14096 (2015).

[29] Y. Xie, Y. Dall'Agnese, M. Naguib, Y. Gogotsi, M. W. Barsoum, H. L. Zhuang, and P. R. C. Kent, Prediction and characterization of mxene nanosheet anodes for non-lithium-ion batteries, ACS Nano **8**, 9606 (2014).

[30] A. Byeon, M.-Q. Zhao, C. E. Ren, J. Halim, S. Kota, P. Urbankowski, B. Anasori, M. W. Barsoum, and Y. Gogotsi, Two-dimensional titanium carbide mxene as a cathode material for hybrid magnesium/lithium-ion batteries, ACS Appl. Mater. Interfaces **9**, 4296 (2017).

[31] D. Er, J. Li, M. Naguib, Y. Gogotsi, and V. B. Shenoy, Ti_3C_2 mxene as a high capacity electrode material for metal (Li, Na, K, Ca) ion batteries, ACS Appl. Mater. Interfaces **6**, 11173 (2014).

[32] D. Cakir, C. Sevik, O. Gulseren, and F. M. Peeters, MO2C as a high capacity anode material: A first-principles study, J. Mater. Chem. A **4**, 6029 (2016).

[33] Q. Tang, Z. Zhou, and P. Shen, Are MXenes Promising Anode Materials for Li Ion Batteries? Computational Studies on Electronic Properties and Li Storage Capability of Ti_3C_2 and Ti_3X_2 (X = F, OH) Monolayer, J. Am. Chem. Soc. **134**, 16909 (2012).

[34] S. Kajiyama, L. Szabova, K. Sodeyama, H. Iinuma, R. Morita, K. Gotoh, Y. Tateyama, M. Okubo, and A. Yamada, Sodium-ion intercalation mechanism in mxene nanosheets, ACS Nano **10**, 3334 (2016).

[35] C. Wang, H. Xie, S. Chen, B. Ge, D. Liu, C. Wu, W. Xu, W. Chu, G. Babu, P. M. Ajayan, and L. Song, Atomic cobalt covalently engineered interlayers for superior lithium-ion storage, Adv. Mater. **30**, 1802525 (2018).

[36] M. R. Lukatskaya, O. Mashtalir, C. E. Ren, Y. Dall'Agnese, P. Rozier, P. L. Taberna, M. Naguib, P. Simon, M. W. Barsoum, and Y. Gogotsi, Cation intercalation and high volumetric capacitance of two-dimensional titanium carbide, Science **341**, 1502 (2013). http://science.sciencemag.org/content/341/6153/1502.full.pdf.

[37] X. Wang, S. Kajiyama, H. Iinuma, E. Hosono, S. Oro, I. Moriguchi, M. Okubo, and A. Yamada, Pseudocapacitance of mxene nanosheets for high-power sodium-ion hybrid capacitors, Nat. Commun. **6**, 6544 (2015).

[38] L. Jian, Y. Xiaotao, L. Cong, Y. Yanquan, X. Le, D. Xin, X. Jinglin, L. Jianhua, and S. Junliang, Achieving high pseudocapacitance of 2D titanium carbide (MXene) by cation intercalation and surface modification, Adv. Energy Mater. **7**, 1602725 (2017).

[39] Q. Hu, D. Sun, Q. Wu, H. Wang, L. Wang, B. Liu, A. Zhou, and J. He, MXene: A new family of promising hydrogen storage medium, J. Phys. Chem. A **117**, 14253 (2013).

[40] F. Shahzad, M. Alhabeb, C. B. Hatter, B. Anasori, S. Man Hong, C. M. Koo, and Y. Gogotsi, Electromagnetic interference shielding with 2D transition metal carbides (MXenes), Science **353**, 1137 (2016). http://science.sciencemag.org/content/353/6304/1137.full.pdf.

[41] X. Bingzhe, Z. Minshen, Z. Wencong, Z. Xu, P. Zengxia, X. Qi, Z. Chunyi, and S. Peng, Ultrathin mxene-micropattern-based field-effect transistor for probing neural activity, Adv. Mater. **28**, 3333 (2016).

[42] M. Khazaei, A. Ranjbar, M. Arai, T. Sasaki, and S. Yunoki, Electronic properties and applications of mxenes: A theoretical review, J. Mater. Chem. C **5**, 2488 (2017).

[43] Z. Ling, C. E. Ren, M.-Q. Zhao, J. Yang, J. M. Giammarco, J. Qiu, M. W. Barsoum, and Y. Gogotsi, Flexible and conductive mxene films and nanocomposites with high capacitance, Proc. Natl. Acad. Sci. **111**, 16676 (2014). http://www.pnas.org/content/111/47/16676.full.pdf.

[44] U. Yorulmaz, A. Ozden, N. K. Perkgoz, F. Ay, and C. Sevik, Vibrational and mechanical properties of single layer mxene structures: A first-principles investigation, Nanotechnology **27**, 335702 (2016).

[45] J. Hui, M. Burgess, J. Zhang, and J. Rodriguez-Lopez, Layer number dependence of Li^+ intercalation on few-layer graphene and electrochemical imaging of its solid–electrolyte interphase evolution, ACS Nano **10**, 4248 (2016). pMID: 26943950.

[46] G. Kresse and J. Furthmüller, Efficiency of *ab initio* total energy calculations for metals and semiconductors using a plane-wave basis set, Comput. Mater. Sci. **6**, 15 (1996).

[47] G. Kresse and J. Furthmüller, Efficient iterative schemes for *ab initio* total-energy calculations using a plane-wave basis set, Phys. Rev. B **54**, 11169 (1996).

[48] J. P. Perdew, K. Burke, and M. Ernzerhof, Generalized gradient approximation made simple, Phys. Rev. Lett. **77**, 3865 (1996).

[49] H. J. Monkhorst and J. D. Pack, Special points for brillouin-zone integrations, Phys. Rev. B **13**, 5188 (1976).

[50] G. Stefan, E. Stephan, and G. Lars, Effect of the damping function in dispersion corrected density functional theory, J. Comput. Chem. **32**, 1456 (2011).

[51] G. Henkelman, B. P. Uberuaga, and H. Jansson, A climbing image nudged elastic band method for finding saddle points and minimum energy paths, J. Chem. Phys. **113**, 9901 (2000).

[52] G. Henkelman and H. Jansson, Improved tangent estimate in the nudged elastic band method for finding minimum energy paths and saddle points, J. Chem. Phys. **113**, 9978 (2000).

[53] W. Tang, E. Sanville, and G. Henkelman, A grid-based bader analysis algorithm without lattice bias, J. Phys.: Condens. Matter. **21**, 084204 (2009).

[54] E. Sanville, S. D. Kenny, R. Smith, and G. Henkelman, An improved grid-based algorithm for bader charge allocation, J. Comp. Chem. **28**, 899 (2007).

[55] G. Henkelman, A. Arnaldsson, and H. Jónsson, A fast and robust algorithm for bader decomposition of charge density, Comput. Mater. Sci. **36**, 254 (2006).

[56] L. Zhao, R. He, K. T. Rim, T. Schiros, K. S. Kim, H. Zhou, C. Gutiérrez, S. P. Chockalingam, C. J. Arguello, L. Pálová, D. Nordlund, M. S. Hybertsen, D. R. Reichman, T. F. Heinz, P. Kim, A. Pinczuk, G. W. Flynn, and A. N. Pasupathy, Visualizing individual nitrogen dopants in monolayer graphene, Science **333**, 999 (2011). http://science.sciencemag.org/content/333/6045/999.full.pdf.

[57] C. Ma, Q. Liao, H. Sun, S. Lei, Y. Zheng, R. Yin, A. Zhao, Q. Li, and B. Wang, Tuning the doping types in graphene sheets by n monoelement, Nano Lett. **18**, 386 (2018).

[58] S. Kawai, S. Saito, S. Osumi, S. Yamaguchi, A. S. Foster, P. Spijker, and E. Meyer, Atomically controlled substitutional boron-doping of graphene nanoribbons, Nat. Commun. **6**, 8098 EP (2015).

[59] N. P. Stadie, E. Billeter, L. Piveteau, K. V. Kravchyk, M. Dobeli, and M. V. Kovalenko, Direct synthesis of bulk boron-doped graphitic carbon, Chem. Mater. **29**, 3211 (2017).

[60] E. Lee and K. A. Persson, Li absorption and intercalation in single layer graphene and few layer graphene by first principles, Nano Lett. **12**, 4624 (2012).

[61] Y. Shaidu, E. Kucukbenli, and S. de Gironcoli, Lithium adsorption on graphene at finite temperature, J. Phys. Chem. C **122**, 20800 (2018).

[62] X.-K. Kong, and Q.-W. Chen, Improved performance of graphene doped with pyridinic N for Li-ion battery: A density functional theory model, Phys. Chem. Chem. Phys. **15**, 12982 (2013).

[63] X. Fan, W. Zheng, and J.-L. Kuo, Adsorption and diffusion of Li on pristine and defective graphene, ACS Appl. Mater. Interfaces **4**, 2432 (2012).

[64] Y.-X. Yu, Can all nitrogen-doped defects improve the performance of graphene anode materials for lithium-ion batteries? Phys. Chem. Chem. Phys. **15**, 16819 (2013).

[65] E. Hazrati, G. A. de Wijs, and G. Brocks, Li intercalation in graphite: A van der waals density-functional study, Phys. Rev. B **90**, 155448 (2014).